Engineering Failure Analysis 126 (2021) 105450

Contents lists available at ScienceDirect

Engineering Failure Analysis

journal homepage: www.elsevier.com/locate/engfailanal

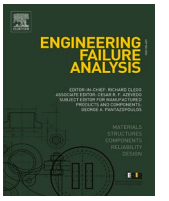

The effect of pearlite morphology and crystallographic texture on environmentally assisted cracking failure

Rodrigo de Carvalho Paes Loureiro [a], Miloslav Beres [a], Mohammad Masoumi [b,*], Hamilton Ferreira Gomes de Abreu [a]

[a] Characterization Laboratory of Materials, Department of Metallurgical and Materials Engineering, Federal University of Ceará, Fortaleza, CE, Brazil

[b] Centro de Engenharia, Modelagem e Ciências Sociais Aplicadas, Universidade Federal do ABC, Santo André, SP 09210-580, Brazil

ARTICLE INFO

Keywords:
Corrosion cracking
Electron backscatter diffraction (EBSD)
Crystallographic orientation
Grain boundary characteristics

ABSTRACT

Mechanism of failure by environmentally assisted cracking was extensively investigated in the present work to find the effect of pearlite morphology and crystallographic texture on crack nucleation and propagation sites. The macrotexture analysis revealed that (0 0 1) crystallographic texture components parallel to the normal direction was predominant in the investigated sample. Crack nucleated at surface pits and propagated in low angle grain boundaries. The refined microstructure prevents crack growth and can deflect crack propagation. High angle grain boundaries were found to suppress crack propagation. In the crack-free region (2 2 3) [1 $\bar{1}$ 0] and ($\bar{1}$ 1 1) [1 $\bar{1}$ 2] texture components were found. Therefore, the control of crystallographic orientation and engineering the grain boundary characteristics can effectively improve the environmentally assisted cracking resistance.

1. Introduction

An excellent combination of high strength, great ductility, and good formability results in the extensive application of cold drawing pearlitic wires. Pearlitic wires find a wide range of applications (flexible pipelines, including suspension bridge cables, automotive tire cords, and cutting wires) due to their excellent tensile strength, hardening capacity, and torsional ductility. These properties are mainly determined by the cementite interlamellar spacing, cementite alignment, residual stress, and proper states of the crystallographic texture of the ferritic matrix [1,2]. The pearlite interlamellar spacing and thickness of cementite lamellae play a significant role in microstructural parameters controlled by thermomechanical processing and microalloying. Cold drawing deformation causes a reduction of the pearlite interlamellar spacing. The use of microalloying elements such as vanadium and chromium to eutectoid composition obtains fine and homogeneous lamellar spacing distribution [3]. The presence of CO_2 in the tensile armor can have deleterious effects on the pearlitic steels. Carbon dioxide can corrode steel, leading to the formation of a corrosive environment and risks of cracking by stress corrosion cracking (SCC) phenomenon [4]. CO_2 corrosion is a complex process because it depends on operational factors such as temperature, pH value, partial CO_2 pressure, flow, and material characteristics [4,5].

Improving the corrosion resistance and suppressing crack nucleation and propagation to extend life expectancy are of interest for the oil, gas, and petrochemical industries. Stress corrosion cracking and hydrogen embrittlement of armor wires or strips deteriorate

* Corresponding author.
E-mail address: mohammad.m@ufabc.edu.br (M. Masoumi).

https://doi.org/10.1016/j.engfailanal.2021.105450
Received 21 December 2020; Received in revised form 26 March 2021; Accepted 26 April 2021
Available online 5 May 2021
1350-6307/

the flexible pipeline's performance by premature failure. It is known that high-strength carbon steel is prone to the hydrogen embrittlement [6,7]. Hydrogen diffusion and entrapment in microstructural defect sites causes hydrogen assisted cracking. The hydrogen assisted cracking strongly depends on chemical composition, microstructure, microstructural defects, strength, and environmental conditions. The hydrogen embrittlement susceptibility can be improved by engineering chemical composition, minimizing the inclusion and segregation, controlling surface roughness, minimizing the number of defects, and avoiding generating stress concentrators. Another approach for the improvement of the hydrogen embrittlement resistance is the engineering of crystallographic texture.

Two types of SCC in pipelines have been defined in the literature: transgranular SCC that is associated with an almost neutral pH, and; intergranular SCC, associated with a high pH [8,9]. The crack initiation and growth in high pH occur by selective dissolution of the grain boundaries. Simultaneously, a passive film forms on the remainder of the surface and on the sides of the cracks that prevent general corrosion at those locations [8]. In neutral pH, SCC is characterized by wide transgranular cracks that occur in regions of the disbonded coatings, which fill with water with a pH around 6.5 [9,10]. Arafin et al. [9] conducted studies, and samples were taken out from an in-service pipeline to analyze the influence of crystallographic texture on the propagation of intergranular stress corrosion (IGSCC) in tubular steel due to high pH. They found that the boundaries of (1 1 0)//rolling plane (RP) and (1 1 1)//RP presents IGSCC resistance, mainly associated with ⟨1 1 0⟩ and ⟨1 1 1⟩ rotation axes, respectively, while the cracked boundaries are mainly linked to the (1 0 0)//RP textured grains. A ⟨1 1 0⟩ fiber texture begins to take shape at the initial stage of a drawing at a drawing strain of 0.63%. Then, this fibre gradually increases its intensity with increasing drawing strain [11]. This is attributed to the formation of a large number of deformation bands and shear-like bands due to the stress concentration at ferrite-cementite interfaces. It is known that ferrite grains with BCC structure in the pearlite colonies are stretched through slip systems (i.e., (1 1 0) ⟨1 1 1⟩, (1 1 2) ⟨1 1 1⟩, and (1 2 3) ⟨1 1 1⟩) during the cold process. Kumar et al. [12] demonstrated that the cementite lamellae tend to reorient themselves along the wire axis. Thus, a variation of cementite morphology such as bending, kinking, thinning of the lamellae is formed with increasing drawing strain.

According the Williamson & Hall's work [13], induced dislocation density effect on the width of diffraction peaks. For instance, the larger peak width obtained by increasing the dislocation density. Although the Rietveld method determine a mean description of full width half maximum (FWHM), it cannot determine the proper crystallographic anisotropy of the phases as suggested by Ungar et al. [14]. Therefore, Ungar et al. [15] proposed a modified Williamson-Hall method to formulate the strain anisotropy by introducing the average contrast factor of dislocation (density). To date, however, the effect of crystallographic texture on stress corrosion cracking susceptibility in addition to hydrogen embrittlement has not been studied satisfactorily. Many researchers studied the corrosion behavior of pearlitic steel in the marine environment [16–19] however, no studies were carried out to investigate the effect of crystallographic orientation on hydrogen embrittlement. Therefore, the effect of pearlite morphology, crystallographic orientation, and grain boundaries on the damage process and life expectancy of flexible pipelines was investigated in this current paper.

2. Material and experimental procedure

The material examined in the present study was a pearlitic steel wire removed from the layer of tensile armour of a flexible pipeline used in the oil and gas industry. The material was thermomechanically processed by rolling and then subjected to torsion deformation. The cross-section of the wire was 6 mm × 14 mm. The chemical composition of the examined material obtained by optical emission spectrometer Shimadzu (model PDA-7000) is shown in Table 1.

2.1. Microstructural characterization

Firstly, the surface of the tensile armour was cleaned with isopropyl alcohol and inspected macroscopically. Then, the section of a sample containing macroscopically visible corrosion products was cut to analyze the corrosion features, the crack extension and the microstructure. Specimens for microstructural analysis were prepared by the standard metallographic preparation method consisting of grinding and polishing using 6, 3, and 1 μm diamond suspension. The sample was then etched for 4–5 s using 4% nital.

Microstructural observations were conducted using a Field Emission Gun Scanning Electron Microscope model FEI® Quanta 450, coupled with Energy Dispersive X-ray Spectrometry (EDS) detector and Electron Backscatter Electron Diffraction (EBSD) detector. Secondary electron and backscatter electron micrographs were acquired at the surface and in the cross-section of the sample. The average size of the ferrite and cementite were measured from the SEM micrographs using Image-J [20] software by means of the linear intercepts method.

2.2. Electron backscatter diffraction (EBSD)

The specimen surfaces were prepared by standard metallographic preparation route, followed by a final polishing step using 0.04

Table 1
Chemical composition of the examined sample (wt.%).

C	Mn	Si	S	P	Cr	Ni	V	Al	Fe
0.7356	0.7597	0.2344	0.0043	0.0152	0.0394	0.0258	0.0045	0.0356	Bal.

μm colloidal silica for 1 h. The EBSD maps were acquired at an operating voltage of 20 kV and a sample tilt angle of 70° using a step size of 100 nm. The Channel 5, MTEX, and ATEX softwares were used to analyze and display the data.

2.3. X-ray diffraction (XRD)

A X'Pert Pro (PANalytical®) diffractometer equipped with Co Kα radiation (λ = 1.79026 Á) operating at 40 kV and 45 mA was utilized for the structural and textural investigation. For the acquisition, the following parameters were used: step size 0.2°, counting time 5 s and the diffraction angle ranged from 45° to 105°. Prior to the XRD measurements, the samples were electropolished at 20 V using a solution of 10 vol-% $HClO_4$ in methanol.

Dislocation density and crystallite size was estimated from the XRD pattern using software package CMWP, developed by Ribárik et al. [21,22].

The CMWP program is based on concepts similar to those of the Rietveld refinement. In the CMWP, the theoretical diffraction pattern is generated, by adding the background function with the profile function [21,22],

$$I_{theoretical} = BG(2\theta) + \Sigma_{hkl} I^{hkl}_{MAX} I^{hkl}(2\theta - 2\theta^{hkl}_0) \quad (1)$$

where BG (2θ) is background function, I^{hkl}_{MAX}, is the peak intensity, $2\theta^{hkl}_0$ is the 2θ value at the peak and I^{hkl}_{MAX} is the theoretical profile function (peak broadening) for the hkl reflection.

The theoretical profile function is expressed by a Fourier transformation obtained by convolution of the measured instrumental profile function, the crystallite size profile function and the strain profile function for dislocations. The instrumental profile function is obtained from a standard sample, the instrumental peaks broadening was determined by LaB6 standard powder sample. The theoretical diffraction pattern is fitted to the experimental data using a least-squares algorithm [21,22].

The theoretical strain profile function is a function of dislocation density, ρ. For dislocated crystals the mean square strain was estimated using approach proposed by Warren and Averbach [23]:

$$A^D(L) = exp\left[-\frac{\pi b^2}{2}(g^2 C)\rho L^2 f\left(\frac{L}{R^*_e}\right) \right] \quad (2)$$

where g is the absolute value of the diffraction vector, L is the displacement of the atoms relative to their ideal position, f is the strain function, b is the absolute value of the Burgers-vector and R^*_e is a length parameter. The C were calculated and measured using the ANIZC program [24] is the contrast factor of the dislocation, which depends on the elastic constants of the material, the orientation, the diffraction vector, the Burgers vector, the line vector and the normal vector of the slip plane of the dislocation.

Before performing the XRD experiments, the samples were electropolished at 20 V using a solution of 10 vol-% HClO4 in methanol. The scanning speed was 0.2° min^{-1}, counting time of 5 s and diffraction angles ranged from 45° to 105°.

The orientation distribution functions (ODFs) were obtained using series expansion method ($I_{max} = 22$), based on the three incompletes {200}, {220} and {211} pole figures, and represented by Bunge convention using three Euler angles $(\varphi_1, \phi, \varphi_2)$.

3. Results and discussion

Fig. 1 shows backscattered scanning electron micrograph acquired from the transversal section of the pearlitic steel wire removed from the tensile armour of a flexible pipeline. Microstructure consists of ferritic matrix with fine cementite lamellae (~80 nm) and partially spheroidized cementite. The presence of spheroidized cementite is an indication that in the course of the fabrication process, the pearlitic steel was maintained above A_{c1} temperature. Moreover, bending and elongation of the cementite lamellae are observed due to the inclined orientation's shear band formation. The formation of nanolaminates ferrite-cementite morphology could be explained by dislocation confinement and dislocation piles-up at the ferrite-cementite interphase.

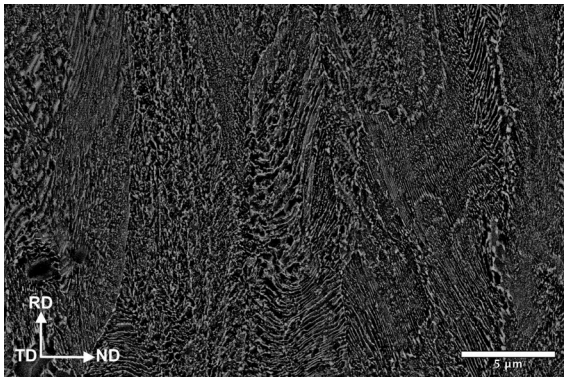

Fig. 1. Backscattered scanning electron micrograph from pearlitic steel wire removed from the tensile armour of a flexible pipeline.

Fig. 2 shows the diffraction profile obtained from the sample's surface. The intense diffraction peaks are associated with (1 1 0), (2 0 0), and (2 1 1) crystallographic planes for the ferritic matrix. At the same time, the cementite phase diffracted the smaller peaks in comparison with ferrite, which is shown enlarged in the selected area. A peak shift to the higher diffraction angle and a peak broadening was observed due to the prior deformation during fabrication and service. This indicates that cementite crystal remains unchanged under external load, unlike the ferrite phase. The dislocation density (ρ) that was estimated from a proper diffraction peak profile analysis is shown in (Table 2). It is to be noted, that the dislocation density of ferrite can also be calculated considering the distance of dislocation walls (dislocation arrangements) by geometrically necessary dislocations using EBSD technique [25]. The ferritic matrix was subjected to compressive and shear stresses during rolling, which induced high-density dislocations walls. Although increased dislocation density contributes to the higher strength of the material via strain hardening mechanism, the interaction between dislocations and carbon in cementite facilitates the dissolution of carbon into ferrite or can lead to cementite decomposition. In other words, increasing the number of the crystallographic defect (i.e., vacancies, dislocations, low and angle boundaries, and interphases) in ferrite due to graduate deformation accelerate the cementite decomposition. The increase in lattice parameter leads to increased lattice distortion, which accommodates higher dislocation densities to trap more cementite carbon, thereby increasing cementite decomposition.

Fig. 3a shows the ODF section at $\varphi_2 = 45^{\circ}$, where intense (0 0 1) crystallographic components parallel to the normal direction (ND) were identified. Additional texture components including (1 1 1)//ND and (1 1 0)//ND appeared in the investigated sample. Skeleton plots for (0 0 1)//ND, (1 1 1)//ND, and (0 1 1)//ND were plotted and presented in Fig. 3b. It is shown that (0 0 1)//ND fiber texture was the most intense texture component, where (0 0 1) [$0\bar{1}0$] (cube component) and (0 0 1) $\langle 1\bar{3}0 \rangle$ components were predominant. The presence of the cube components is an indication that the sample was processed by hot rolling. Also, this texture was maintained after subsequent post-deformation steps during the production of the final product and even in-service conditions.

Our results indicate that the post-deformation was not sufficient to eliminate the dendritic structure entirely. Also, the rotated cube texture component (1 0 0) $\langle 1 3 0 \rangle$ within 15° deviation from the cube component exhibits low cleavage resistance against crack propagation [26]. It is notable that (1 1 0) $\langle 1 1 1 \rangle$ and (1 1 1) $\langle 1 1 0 \rangle$ also were dominated, are laid in the compact planes and direction in BCC crystal (i.e., Compact planes are {1 1 0}, {1 1 2} and {1 2 3} and compact direction is $\langle 1 1 1 \rangle$ of BCC crystals). Holscher et al. [27] explained that the formation of (1 1 1) $\langle u v w \rangle$ components originated from a 30°$\langle 1 1 1 \rangle$ rotation, as well as the 35°$\langle 1 1 0 \rangle$ orientation relationship, which mainly occurred in cold-formed steels.

It is known that the preferred growth direction of dendrites in cubic crystals is $\langle 1 0 0 \rangle$ direction, which is caused by solidification conditions and the direction of the heat flow [28]. A remarkable reduction in mechanical properties and corrosion behavior were reported in the as-cast state. At the same time, deformation is essential to refine microstructure, which improves mechanical properties by introducing more obstacles to slip in line with the Hall–Petch relation.

During cyclic loading in a corrosive environment, corrosion fatigue can occur. Here, crack mainly initiates at the surface at corrosion pits and then propagates in the component's depth. The corrosion pits are formed on the surface due to anodic and cathodic reactions exposed to the humid and corrosive environment during the service. In this scenario, pits localize anodic dissolution and/or hydrogen embrittlement, causing the pits coalescence coupled with cyclic loading to enhance the transition from corrosion pits to crack growth [29]. When the crack size becomes large enough, eventually, a rupture will occur. Fig. 4 exhibits the pits mainly initiate cracks near the surface where local plastic deformation occurs, accompanied by nonmetallic inclusions and strain accumulation to promote pits to crack transition by coalescing small pits and cracks from the main crack. Besides, surface defects/damages (i.e., scratches, grinding, roughness, debris indentations, etc.) also increase stress concentration, accelerating pits-to-crack transition the stress corrosion cracks become more accented than local electrode potential.

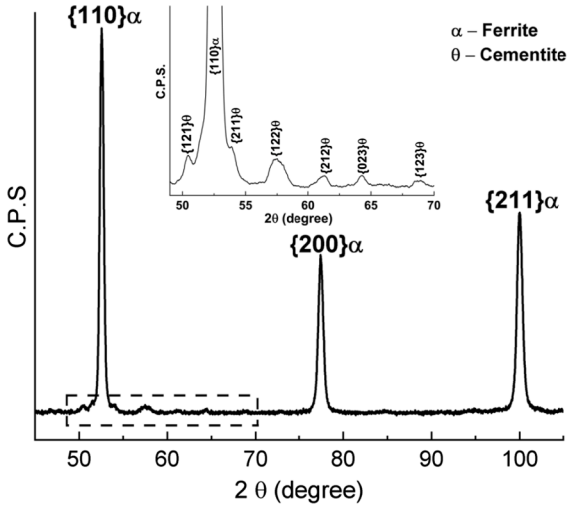

Fig. 2. XRD diffraction profile obtained from the rolled and distorted pearlitic sample.

Table 2
FWHM, lattice parameters and dislocation density obtained from the XRD analysis.

Peak Position (Degree)	h	k	l	FWHM	d-spacing (Å)	a_{hkl}(Å)	$\rho(m^{-2})$
52.57	1	1	0	0.53083	2.0212	2.8585	6.2×10^{13}
77.46	2	0	0	0.69692	1.4307	2.8614	
100.00	2	1	1	0.76142	1.1685	2.8621	

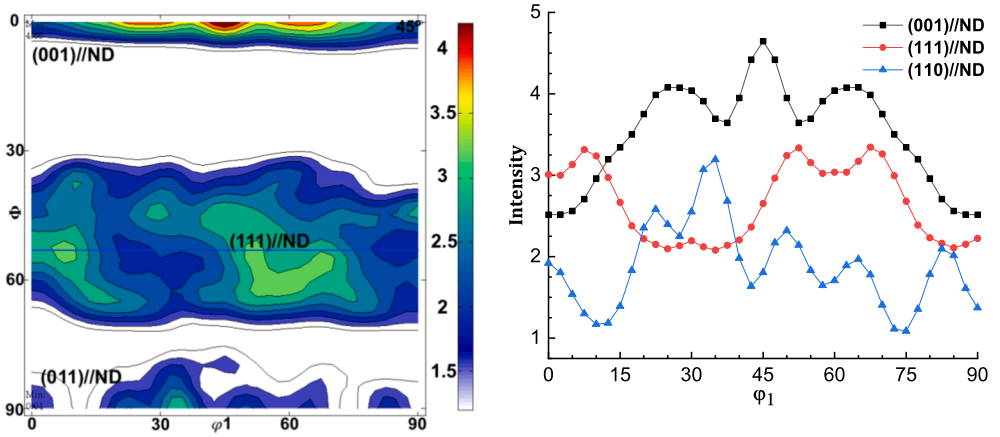

Fig. 3. (a) Texture components in a constant $\varphi_{2=45^{\circ}}$ section of the ODF and (b) skeleton plots for (001)//ND, (111)//ND, and (011)//ND components.

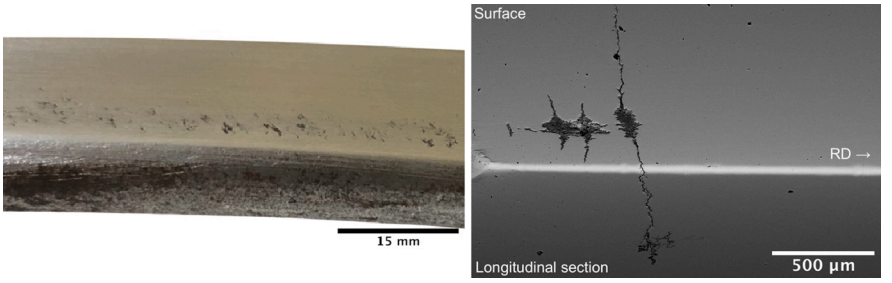

Fig. 4. Pit corrosions presence on the external surface of the rolled and distorted pearlitic sample.

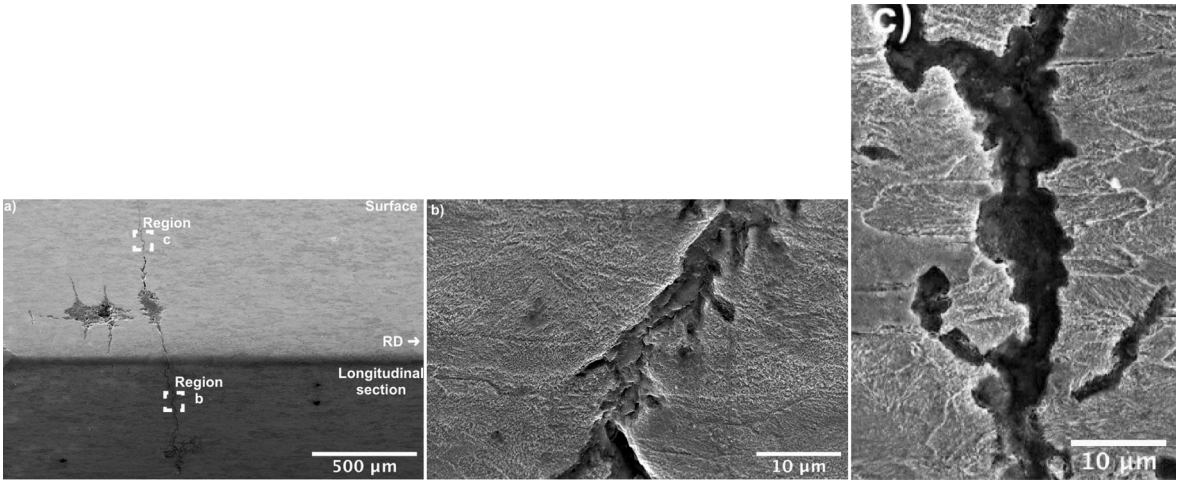

Fig. 5. Crack growth in complex transgranular and intergranular cracking mode and crack deflection at grain boundaries.

Pits corrosions were found on the surface because of hydrogen escaping and the distribution of corrosion products. Nonmetallic inclusions such as MnS and complex oxides can accelerate the corrosion reaction. In particular, Mn inclusions on the surface could lead to pitting corrosion. It is suggested that a Mn^{2+} formed by chemical dissolution, coupled with the formation of H_2S, in humid and corrosive (HCO_3) condition, via reaction:

$$MnS + H^+ \rightarrow Mn^{2+} + H_2S \quad (1)$$

Furthermore, the dissolution of MnS in the acidic-humid environment exacerbates the aggressiveness of the solution. Thereby, it accelerates the transition from pit to crack to the anodic dissolution accompanied by highly stresses localized regions below the pit mouth, which governed the transition from pit to stress corrosion crack [18] propagation rate could be different due to stress distribution and corrosive environment.

The combination of varying cyclic loads in the presence of an aggressive environment leads to corrosion crack initiation, which originates from the pit corrosion at the surface. Then, the crack would propagate into the bulk. Fig. 5 shows the trajectory of crack growth in complex transgranular and intergranular cracking mode and crack deflection at grain boundaries. It is well-known that microstructure plays an essential role in crack propagation. For instance, hard and brittle phases facilitate crack propagation. Also, the ferrite-cementite interphase eases the crack propagation, leading to the crack type becomes intergranular. The transition from a pit to a crack depends on the size and shape factor. Our results revealed that corrosion crack initiated from the corrosion pits, while pits nucleate from sulfide precipitates observed at the surface. A humid environment increases the corrosion rate while operating temperature and pressure enhance the formation of a saturated solution such as salt, chlorides, and sulphuric acid. This saturated solution at the steel surface can promote corrosion pits [30].

In contrast, the repeated tension and torsion cycles at operating temperature increase accumulate stress on the grain boundaries at the surface and resulting in branching crack propagation. A ramified cracking containing the corrosion products clearly shows in Fig. 5, which was nucleated from pit corrosion on the surface. Also, some multiple cracks were observed during metallographic examination with a maximum depth of ~1500 μm.

The local severe plastic deformation mostly at the ferrite-cementite interface generates the shear deformation, thereby, increasing the rate of crack growth. It is known that pearlite morphology, ferritic matrix crystallographic texture, ferrite-cementite interface, and residual stress determine the mechanical properties. Khan et al. [31] reported that the proper microstructural tailoring and corresponding axial alignment can significantly decrease the corrosion rate in chloride solution. They also showed that ferrite-cementite interface acts as main place micro-galvanic corrosion due to the dislocations misfit at the ferrite-cementite interface. Mehtani et al. [32] also investigated the influence of interface crystallography on oxidation kinetics in pearlitic steels. They showed that lower interface energy as a result of higher degree of alignment at the ferrite-cementite interface, led to the lower oxidation kinetics due to the reduction of residual stresses. Arafin et al. [33] claimed that high angle grain boundaries provide an easy path for crack propagation. In contrast, low angle boundaries having a low energy were not favorable for the stress corossion crack propagation.

Fig. 6 shows the EDS map for Fe and O and confirmed the presence of oxide products in the crack path. A higher level of oxygen at the crack path suggested the presence of oxide production (i.e., iron carbonate and iron oxide) within a relatively large crack trajectory. Microstructural observation exhibits the chemo-mechanical coupling due to the high oxygen and water during the operating process, which cracks oxidations cover the surface. This figure also confirmed the cementite fragmentation in the crack path's vicinity due to localized stress/plastic strain in CO_2-containing aqueous environments. The crack tends to pass through the grains and broken cementite particles and/or deflected from the cementite particles. It is notable that crack- particle interactions are highly affected by localized stress/plastic strain.

The electron backscattered diffraction (EBSD) technique was employed to investigate environmentally assisted cracking in the present sample. EBSD analyses can provide evidence to explain the mechanics-based for local crack initiation from pits according to the strain accumulation by stress corrosion cracks mechanism. The orientation image maps (OIMs) in three distinct areas (i) crack-free, (ii) crack-path, and (iii) crack-arrest, were measured and presented in Fig. 7 to investigate the effect of crystallographic orientation and stress distribution in grains directions on crack propagation and arrest. The grain orientations are colored as given in the triangular

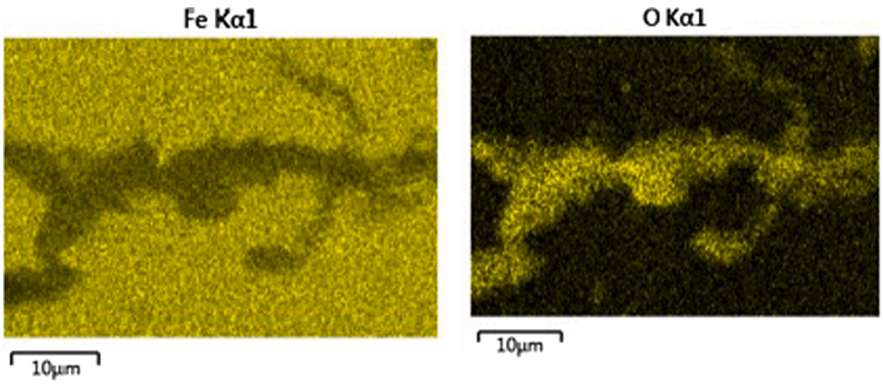

Fig. 6. EDS map from the area shown in Fig. 5c, revealing presence of oxygen in the crack.

legend corresponding to the crystallographic orientation distribution (ND axis corresponding to the Z-axis). The low, medium, and high angle boundaries (LABs, MABs, and HABs), defined here as misorientations 2°–5°, 5°–15°, and greater than 15° respectively, are highlighted as black lines. The average grain sizes in three distinct regions were about 0.65, 3.85, and 0.75 ± 0.25 μm in crack-free, crack-path, and crack-arrest, respectively. It is well known that the yield stress increases with decreasing grain size by the Hall-Petch effect due to the formation of dislocation pile-up and the energy barrier for dislocation movement, improving mechanical properties.

The crystallographic orientation distribution was measured individually and presented as normal (or z) direction inverse pole figures (IPFs) map in Fig. 8. The grains oriented along (1 1 1) planes parallel to the normal direction were predominant in the crack-free region, while (0 0 1) grains with deviation about 35.5° and 28.5° were oriented in crack-path and crack-arrest regions, respectively.

The distribution of point-to-point angle misorientation and boundaries classification following misorientation within the range from 2°–5°, 5°–15°, and 15-62° of all investigated specimens were shown in Fig. 9 and listed in Table 3. The crack-free region exhibits the highest high angle boundaries (HABs) with the point-to-point misorientation greater than 15°. The highest fraction of HABs was attributed to the ultrafine grains formed in this region. Also, HABs act as energy barriers to prevent crack initiation and crack propagation. However, the fraction of low and medium angle boundaries (LABs and MABs) was highest in the cracked regions due to crystallographic lattice distortion within the grains. There is a close relationship between dislocation densities and the volumetric fraction of LABs in crystalline materials. The highest volumetric fraction of LABs in the crack-path region could be associated with the high dislocation density and highly deformed region generated by the crack tip plastic zone, which provides an easy path for trans-granular crack propagation. Moreover, the high dislocation densities accompanied by favored {1 1 2} slip plans in the crack-arrest region; facilitate the formation of subgrains (MABs). Thereby, crack deflections and branches would occur in the presence of sub-grains, caused a reduction in crack growth rate, and finally, the crack would arrest over a short distance.

In general, pearlite morphology and alignment at the ferrite-cementite interface influences the crack growth [11,12]. Uniformly distributed pearlite colony with no preferential texture can deflect and disturb crack propagation, while aligned pearlite colonies along drawing direction can provide a straight crack path. Several authors reported that homogeneous and uniform ferrite-pearlite structure has higher stress corrosion resistance. King et al. [13] claimed that the grain boundaries with low index $\{hkl\}$ planes are crack-resistant for intergranular stress corrosion cracking. In addition, the crack growth rate is associated with the local plastic deformation zone, which is governed by grain boundaries characteristics and ferrite/cementite interface. According to the Arafin et al. [10] reports and our results, it was found that grains with orientations close to the (1 1 0)//rolling plane with a good-fit crystallographic interface, suppressing environmentally assisted cracking. On the other hand, the (0 0 1) grains with the highest interface misfit are preferred sites for dislocation and strain concentration, enhancing the environmentally assisted cracking initiation.

Hayden et al. [14] found that in low-carbon steel, localized corrosion initiated at cementite ferrite interface. Beside the effect of ferrite-cementite interface crystallography [15–17], the ferritic grain boundaries and ferrite crystallographic texture are also important in hydrogen trapping phenomena. The high-angle grain boundaries are considered as irreversible hydrogen traps include non-metallic inclusions and precipitates due to high stored energy induced by lattice distortion [18]. Low-angle grain boundaries and dislocations are also classified as weak or reversible hydrogen traps [19]. The efficiency of hydrogen traps at crystalline defects associated with atomic arrangements and atomic spacing associated with crystallographic orientation has been studied [20,21]. For instance, semi-coherent interface with misfit dislocations mainly formed in less atomic compact crystalline planes and direction, indicating the deep hydrogen trapping. Ogawa et al. [22] also reported that, the preferential initiation sites of hydrogen-induced,

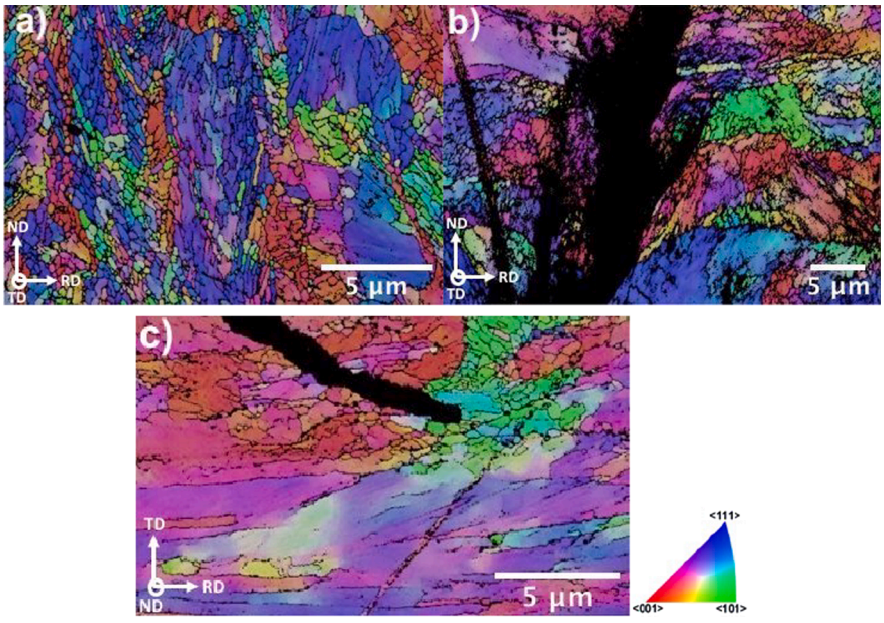

Fig. 7. Normal direction orientation image maps (OIMs) in three distinct areas (a) crack-free, (b) crack-path, and (c) crack-arrest.

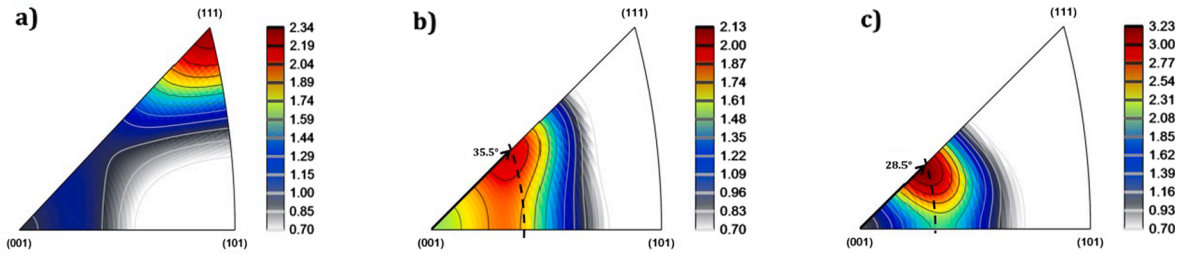

Fig. 8. Normal (or z) direction inverse pole figures (IPFs) map in three distinct areas (a) crack-free, (b) crack-path, and (c) crack-arrest.

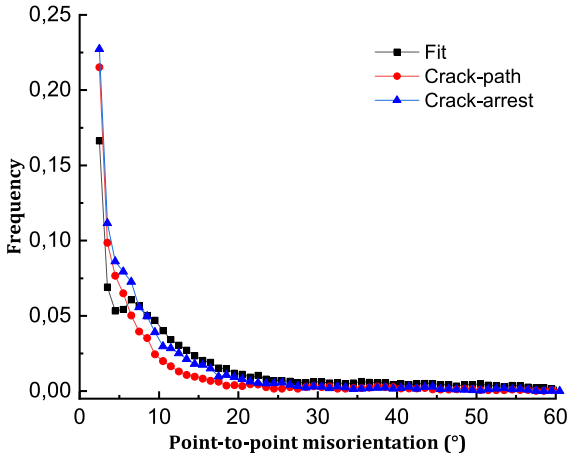

Fig. 9. Distribution of point-to-point angle misorientation.

Table 3
Grain boundary characteristics classified into low angle boundaries (LABs), Medium angle boundaries (MABs) and high angle boundaries (HABs) in three distinct regions.

	Crack-free	Crack-path	Crack-arrest
LABs ($2^\circ < \theta < 5^\circ$)	28.77	50.24	42.33
MABs ($5^\circ < \theta < 15^\circ$)	44.32	37.65	43.50
HABs ($15^\circ < \theta$)	26.91	12.11	14.17

surface micro-cracks were the ferrite/cementite lamellar aligned nearly parallel to the tensile loading axis.

Fig. 10 exhibits the Schmid factor maps for each individual grain orientation to the loading direction of three distinct investigated regions analyzed by EBSD technique. Plastic deformation is governed by the Schmid factor values' variation coupled with activated slip systems [26]. Crack-free region presented the lowest Schmid factor values among all regions. A lower Schmid factor could be shown a lower tendency for activated slip systems, increasing the local stress concentration and increasing the microhardness. This could be resulted that the probable micro-crack would encounter the barrier to growth. Therefore, a more uniform strain distribution would result in this region, leading to grain refinement as shown previously. The higher Schmid factor values in cracked regions present a higher tendency for activated slip systems and less barrier energy for crack growth under external loading. The analyses of grain crystallographic orientations in {1 1 0} slip systems of BCC structure were also carried out using the ATEX analysis software. The corresponding volume fractions for each slip system for the family of {1 1 0} ⟨1 1 1⟩ as main slip system in BCC lattice are listed in Table 4. It can be seen that (1 0 1) [1 $\bar{1}$ $\bar{1}$] slip system is the main slip system in both crack-free and crack-free regions, which could be noted as a favorable slip system. It is also noted that (1 0 1) [1 $\bar{1}$ $\bar{1}$] slip system has a substantially large volume fraction of 83.64%.

The orientation distribution function (ODF), which represents normalized probability density associated with given crystal orientation in material, was used to describe the grains' preferred orientation in analyzed regions. The ODF at constant $\varphi_2 = 45^\circ$ section is presented in Fig. 11. The crack-free region revealed the (2 2 3) [1 0 $\bar{1}$] and ($\bar{1}$ 1 1) [1 2 $\bar{1}$] components. The (2 2 3) [1 0 $\bar{1}$] component in α-fibre was observed in recrystallized ferrite and spherical cementite of a medium carbon steel during cold rolling and subsequent recrystallization [34,35]. The ($\bar{1}$ 1 1) [1 2 $\bar{1}$] component along the γ-fiber is also formed by deep-drawing with {1 1 1} or {1 1 2} orientations mainly by twinning depending upon the configuration of slip systems following the recrystallization stage due to the level of dislocation density in comparison with neighboring areas, which enhance its growth [36]. During operating, external stress

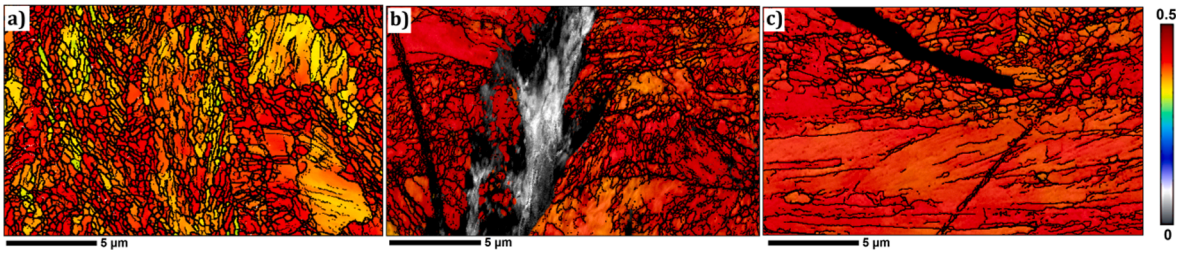

Fig. 10. Schmid factor maps in three distinct areas (a) crack-free, (b) crack-path, and (c) crack-arrest.

Table 4
Slip systems and their corresponding volume fractions.

Slip system	Fraction		
	Crack-free	Crack-path	Crack-arrest
(0 1 1) [1 1 $\bar{1}$]	0.13	0.14	0.06
(1 0 1) [1 1 $\bar{1}$]	0.03	0.15	0.01
(1 $\bar{1}$ 0) [1 1 $\bar{1}$]	0	0	0
(0 1 $\bar{1}$) [1 $\bar{1}$ 1]	0.19	0.10	0.03
(1 0 1) [1 $\bar{1}$ $\bar{1}$]	32.48	15.94	83.64
(1 1 0) [1 $\bar{1}$ $\bar{1}$]	6.38	15.36	1.32
(0 1 1) [1 $\bar{1}$ 1]	27.61	30.82	6.66
(1 0 $\bar{1}$) [1 $\bar{1}$ 1]	1.16	0.01	1.21
(1 1 0) [1 $\bar{1}$ 1]	17.76	23.01	2.26
(0 1 $\bar{1}$) [1 1 1]	9.93	3.08	3.95
(1 0 $\bar{1}$) [1 1 1]	4.30	11.39	0.87
(1 $\bar{1}$ 0) [1 1 1]	0	0	0

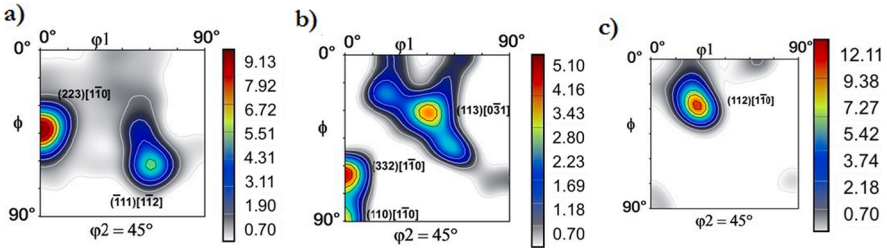

Fig. 11. Texture components in a constant$\varphi_{2=45^\circ}$ section of the ODF obtained from EBSD data (a) crack-free, (b) crack-path, and (c) crack-arrest.

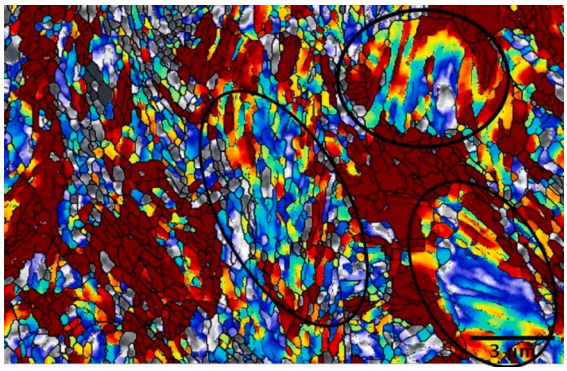

Fig. 12. Local strain distribution developed in-grains calculated by kernel-based methods from EBSD data (Fig. 7a).

generates internal or stored by lattice curvature, which affects neighboring grains and accommodates plastic deformation on active slip systems to relieve stress concentration. This plastic deformation can also be restricted, thereby the local slip-on strain consistency would generate. Thus, crystal orientation could be changed in accordance with the active slip systems. Recently, Zhang et al. [37] reported that {1 1 1} ⟨1 1 2⟩ texture becomes weaker {1 1 1} ⟨1 1 2⟩ texture led to re-orientation into {1 1 1} ⟨1 1 0⟩ component, and then transits to {1 1 2} ⟨1 1 0⟩ orientation. Therefore, the external load can consume by crystallographic orientation changes, rather than the formation of lattice defects and stress concentration sites. Fig. 12 shows the distribution of the residual strain within the grain characterizing by Kernel-based methods. It is clearly shown ferritic matrix grains are oriented along ⟨1 1 1⟩ direction (Fig. 7a) as the main slip direction in the BCC structure provides adequate slips systems for dislocation motion. Thus, a smooth strain distribution developed in these grains, which is highlighted by black circles in Fig. 12. While the local strain pile-up due to the dislocation accumulation was developed in grains mainly laid in ⟨0 0 1⟩ direction as the largest interatomic spacing due to the lack of available slip systems. On the other hand, a significant amount of dislocation can be arranged according to the different active slip systems in neighboring lattices, leading to the deformation bands' formation. This can be responsible for grain refinement in ⟨0 0 1⟩ grains.

Furthermore, the (1 1 3)[0 $\bar{3}$ 1], (3 3 2) [1 0 $\bar{1}$], and (1 1 0) [1 0 $\bar{1}$] texture components were characterized at crack trajectory, represents preferred sites with high stored energy for crack propagation. Dillamore et al. [38] stated that the number of texture components near [0 3 1] direction increases with reducing the temperature of BCC structure, which twin system became predominant. Thus, temperature-dependence crystal orientation concentrates excessive stacking fault energy, which facilitates crack growth as well. Shan et al. [39] reported that the presence of (3 3 2) [1 0 $\bar{1}$] component with 20° deviation from accurate γ fiber ({1 1 1}//ND) in the vicinity of crack initiation in the shear bands. Finally, the rotated Goss (0 1 1) [1 1 0] texture components formed by ingrain shear bands with Cube orientation (i.e., (0 0 1) [1 1 0]) [40], increasing the anisotropy and deteriorates the mechanical properties. Better understanding of the crack-arrest microstructure can help us to provide excellent crack-arrestability materials to enhance ductility. The ultrafine 0.75 ± 0.25 μm polygonal ferrite with (1 1 2) [1 0 $\bar{1}$] predominant texture component formed during hot rolling, were characterized in this region. The refined microstructure prevents crack growth and can deflect crack propagation. The (1 1 2) components can generally improve low-temperature toughness, accompanied with elimination of the cleavage {0 0 1} and {1 1 0} slip planes to promote low-temperature fracture [41].

Durgaprasad et al. [23] reported that ferrite-cementite interface, subjected to heavy wire drawing and/or annealing, may have sharp or diffused carbon distribution, which may affect the environmentally assisted cracking. In this scenario, delamination is mainly associated with the cementite decomposition (drawing strain higher than 5.0), results in increasing of carbon concentration in the ferrite. The higher carbon content in ferrite causes its higher hardness and loss of ductility, even forming the nanoscale carbon-supersaturated ferrite. Therefore, it is expected that local severe plastic deformation mostly at the ferrite-cementite interface generates the shear deformation, thereby, increasing the rate of crack growth.

4. Conclusion

The effect of pearlite morphology and crystallographic texture on environmentally assisted cracking failure in a pearlitic steel wire was investigated comprehensively, to introduce the influence of microstructure morphology, crystallographic orientation, and the grain boundary characteristics in improvement of the environmentally assisted cracking resistance. The following results were obtained;

- The cementite lamella underwent bending and elongation due to the inclined orientation's shear band formation during the fabrication and the operating process.
- Corrosion cracks mainly nucleate from pit corrosion on the surface due to anodic and cathodic reactions, and then propagate in the component's depth.
- The presence of low cleavage resistance (0 0 1)//ND fiber texture in the investigated sample facilitates the initiation and propagation of corrosion cracks.
- Corrosion cracks propagated along the low angle grain boundaries, while high angle grain boundaries were found to suppress crack propagation.
- Local dislocation accumulation developed in grains mainly laid in ⟨0 0 1⟩ direction as the largest interatomic spacing caused the grain refinement.
- In the crack-free region (2 2 3) [1 0 $\bar{1}$] and ($\bar{1}$ 1 1) [1 2 $\bar{1}$] texture components were found.

Declaration of Competing Interest

The authors declare that they have no known competing financial interests or personal relationships that could have appeared to influence the work reported in this paper.

Acknowledgement

The authors acknowledge the Brazilian research agencies; CNPq, the research board of the Universidade Federal do Ceará for the financial support and Laboratório de Caracterização de Materiais (LACAM) and Central Analytical (CT-INFRA/MCTI-SISNAD) for provision of research facilities of this work.

References

[1] M. Masoumi, L. Flavio, G. Herculano, R. De Carvalho, P. Loureiro, H.F. Gomes, M. Be, D. Abreu, M. Masoumi, C. De Engenharia, L. Flavio, G. Herculano, R.D. C. Paes, H. Ferreira, G. De Abreu, Microstructure and Crystallographic Texture Changes under Torsion Loading of Pearlitic Steel Strips, J. Mater. Eng. Perform. 29 (2020) 7250–7259, https://doi.org/10.1007/s11665-020-05232-8.

[2] A. Durgaprasad, S. Giri, S. Lenka, S. Kundu, S. Mishra, S. Chandra, R.D. Doherty, I. Samajdar, Defining a relationship between pearlite morphology and ferrite crystallographic orientation, Acta Mater. 129 (2017) 278–289.

[3] K. Han, T.D. Mottishaw, G.D.W. Smith, D.V. Edmonds, A.G. Stacey, Effects of vanadium additions on microstructure and hardness of hypereutectoid pearlitic steels, Mater. Sci. Eng. A. 190 (1-2) (1995) 207–214.

[4] C. Taravel-condat, N. Desamais, Qualification of High Strength Carbon Steel Wires for Use in Specific Annulus Environment of Flexible Pipes Containing CO2 and H2S, Mater. Sci. 13 (2006) 961, https://doi.org/10.1115/OMAE2006-92394.

[5] S. Nešić, Key issues related to modelling of internal corrosion of oil and gas pipelines – A review, Corros. Sci. 49 (12) (2007) 4308–4338, https://doi.org/10.1016/j.corsci.2007.06.006.

[6] S.K. Sharma, S. Maheshwari, A review on welding of high strength oil and gas pipeline steels, J. Nat. Gas Sci. Eng. 38 (2017) 203–217, https://doi.org/10.1016/j.jngse.2016.12.039.

[7] M. Masoumi, S.S.M. Tavares, J.M. Pardal, T.R.B. Martins, M.J. Gomes da Silva, H.F.G. de Abreu, The role of microstructure and grain orientations on intergranular cracking susceptibility of UNS 17400 martensitic stainless steel, Eng. Fail. Anal. 79 (2017) 198–207, https://doi.org/10.1016/j.engfailanal.2017.04.008.

[8] E. Ohaeri, U. Eduok, J. Szpunar, Hydrogen related degradation in pipeline steel: A review, Hydrog. Energy. 43 (2018) 14584–14617.

[9] M.A. Arafin, J.A. Szpunar, A new understanding of intergranular stress corrosion cracking resistance of pipeline steel through grain boundary character and crystallographic texture studies, Corros. Sci. 51 (2009) 119–128, https://doi.org/10.1016/j.corsci.2008.10.006.

[10] A. Eslami, B. Fang, R. Kania, B. Worthingham, J. Been, R. Eadie, W. Chen, Stress corrosion cracking initiation under the disbonded coating of pipeline steel in near-neutral pH environment, Corros. Sci. 52 (11) (2010) 3750–3756, https://doi.org/10.1016/j.corsci.2010.07.025.

[11] N. Guo, BaiFeng Luan, BingShu Wang, Q. Liu, Microstructure and texture evolution in fully pearlitic steel during wire drawing, Sci. China Technol. Sci. 56 (5) (2013) 1139–1146, https://doi.org/10.1007/s11431-013-5184-7.

[12] P. Kumar, N.P. Gurao, A. Haldar, S. Suwas, Progressive Changes in the Microstructure and Texture in Pearlitic Steel during Wire Drawing, ISIJ Int. 51 (4) (2011) 679–684.

[13] G.K. Williamson, W.H. Hall, X-ray line broadening from filed aluminium and wolfram, Acta Metall. 1 (1) (1953) 22–31, https://doi.org/10.1016/0001-6160(53)90006-6.

[14] T. Ungár, Dislocation densities, arrangements and character from X-ray diffraction experiments, Mater. Sci. Eng. A. 309-310 (2001) 14–22.

[15] T. Ungár, A. Borbély, The effect of Dislocation Contrast on x-ray Line Broadening: A new Approach to Line Profile Analysis, Appl. Phys. Lett. 69 (21) (1996) 3173–3175, https://doi.org/10.1063/1.117951.

[16] S.W. Joung, U.G. Kang, S.P. Hong, Y.W. Kim, W.J. Nam, Aging behavior and delamination in cold drawn and post-deformation annealed hyper-eutectoid steel wires, Mater. Sci. Eng. A. 586 (2013) 171–177, https://doi.org/10.1016/j.msea.2013.07.095.

[17] E.V. Chatzidouros, V.J. Papazoglou, T.E. Tsiourva, D.I. Pantelis, Hydrogen effect on fracture toughness of pipeline steel welds, with in situ hydrogen charging, Int. J. Hydrogen Energy. 36 (19) (2011) 12626–12643, https://doi.org/10.1016/j.ijhydene.2011.06.140.

[18] L. Wang, J. Xin, L. Cheng, K. Zhao, B. Sun, J. Li, X. Wang, Z. Cui, Influence of inclusions on initiation of pitting corrosion and stress corrosion cracking of X70 steel in near-neutral pH environment, Corros. Sci. 147 (2019) 108–127.

[19] G. Ghosh, P. Rostron, R. Garg, A. Panday, Hydrogen induced cracking of pipeline and pressure vessel steels: A review, Eng. Fract. Mech. J. 199 (2018) 609–618.

[20] S.A. Bankole, J. Buckman, D. Stow, H. Lever, Grain-size analysis of mudrocks : A new semi-automated method from SEM images, J. Pet. Sci. Eng. 174 (2019) 244–256, https://doi.org/10.1016/j.petrol.2018.11.027.

[21] G. Ribárik, J. Gubicza, T. Ungár, Correlation between strength and microstructure of ball-milled Al–Mg alloys determined by X-ray diffraction, Mater. Sci. Eng. A. 387–389 (2004) 343–347, https://doi.org/10.1016/j.msea.2004.01.089.

[22] G. Ribárik, T. Ungár, J. Gubicza, MWP-fit: A program for multiple whole-profile fitting of diffraction peak profiles by ab initio theoretical functions, J. Appl. Crystallogr. 34 (5) (2001) 669–676, https://doi.org/10.1107/S0021889801011451.

[23] B.E. Warren, B.L. Avebach, The Separation of Cold-Work Distortion and Particle Size Broadening in X-Ray Patterns, J. Appl. Phys. 23 (1952) 17022, https://doi.org/10.1063/1.1702234.

[24] A. Borbély, J. Dragomir-Cernatescu, G. Ribárik, T. Ungár, Computer program ANIZC for the calculation of diffraction contrast factors of dislocations in elastically anisotropic cubic, hexagonal and trigonal crystals, J. Appl. Crystallogr. 36 (1) (2003) 160–162, https://doi.org/10.1107/S0021889802021581.

[25] S. Sato, K. Wagatsuma, M. Ishikuro, E.-P. Kwon, H. Tashiro, S. Suzuki, Precise Characterization of Dislocations and Cementite in Pearlitic Steels at Different Drawing Strains Using X-ray Diffraction, ISIJ Int. 53 (4) (2013) 673–679.

[26] M. Masoumi, C.C. Silva, M. Béreš, D.H. Ladino, H.F.G. de Abreu, Role of crystallographic texture on the improvement of hydrogen-induced crack resistance in API 5L X70 pipeline steel, Int. J. Hydrogen Energy. 42 (2) (2017) 1318–1326, https://doi.org/10.1016/j.ijhydene.2016.10.124.

[27] M. Holscher, D. Raabe, K. Lucke, Rolling and recrystallization texture of bcc steels, Mater. Technol. - Steel Res. 62 (1991) 567–575.

[28] Y. Natsume, K. Ohsasa, H. Esaka, T. Narita, Analysis of Growth Behavior of a Cellular and Dendritic Interface under a Constrained Growth Condition using a Phase-Field Model, Mater. Trans. 44 (2003) 824–828.

[29] B.T. Lu, J.L. Luo, Crack Initiation and Early Propagation of X70 Steel in Simulated Near-Neutral pH Groundwater, Corros. Eng. 62 (8) (2006) 723–731, https://doi.org/10.5006/1.3278297.

[30] P. Roffey, E.H. Davies, The generation of corrosion under insulation and stress corrosion cracking due to sulphide stress cracking in an austenitic stainless steel hydrocarbon gas pipeline, Eng. Fail. Anal. 44 (2014) 148–157, https://doi.org/10.1016/j.engfailanal.2014.05.004.

[31] M.I. Khan, H.K. Mehtani, A. Durgaprasad, G.K. Goyal, M.J.N.V. Prasad, S. Parida, T. Dasgupta, N. Birbilis, I. Samajdar, The defining role of interface crystallography in corrPhiosion of a two-phase pearlitic steel, Philos. Mag. 100 (2020) 1439–1453, https://doi.org/10.1080/14786435.2020.1725247.

[32] H.K. Mehtani, M.I. Khan, A. Durgaprasad, S.K. Deb, S. Parida, M.J.N.V. Prasad, I. Samajdar, Oxidation kinetics in pearlite: The de fi ning role of interface crystallography, Scr. Mater. 152 (2018) 44–48, https://doi.org/10.1016/j.scriptamat.2018.04.011.

[33] M.A. Arafin, J.A. Szpunar, A new understanding of intergranular stress corrosion cracking resistance of pipeline steel through grain boundary character and crystallographic texture studies, Corros. Sci. 51 (2009) 119–128, https://doi.org/10.1016/j.corsci.2008.10.006.

[34] Y.M. Yu, Y.B. Xu, C.S. Li, G.D. Wang, Effects of cold rolling on crystallographic texture of oriented silicon steel produced by TSCR, Mater. Res. Innov. 15 (2011) 274–277, https://doi.org/10.1179/143307511X12858957673996.

[35] C. Herrera, N.B. Lima, A.F. Filho, R.L. Plaut, A.F. Padilha, Texture and mechanical properties evolution of a deep drawing medium carbon steel during cold rolling and subsequent recrystallization, J. Mater. Process. Technol. 209 (2009) 3518–3524, https://doi.org/10.1016/j.jmatprotec.2008.08.007.

[36] G.M. Rusakov, A.A. Redikultsev, M.L. Lobanov, Formation Mechanism for the Orientation Relationship between {110}h001i and {111}h112i Grains during Twinning in Fe-3 Pct Si Alloy, Metall. Mater. Trans. A. 39 (2008) 2278–2280, https://doi.org/10.1007/s11661-008-9575-5.

[37] C.B.C.C. Steel, S. Model, Study on Texture and Grain Orientation Evolution in Cold-Rolled BCC Steel by Reaction Stress Model, Crystals. 10 (2020) 680–693, https://doi.org/10.3390/cryst10080680.

[38] I. Dillamore, W. Roberts, Preferred Orientation in Wrought abd Annealed Metals, Metall. Rev. 10 (1965) 110.

[39] N. Shan, J. Liu, Y. Sha, F. Zhang, L. Zuo, Fabrication of Fe-2.1 wt.% Si Alloy Sheets with Dominant Goss Texture Through Thickness, Mater. Res. 22 (2019) 20180757.
[40] H. Jiao, Y. Xu, L. Zhao, R.D.K. Misra, Y. Tang, D. Liu, Y. Hu, M. Zhao, M. Shen, Texture evolution in twin-roll strip cast non-oriented electrical steel with strong Cube and Goss texture, Acta Mater. 199 (2020) 311–325, https://doi.org/10.1016/j.actamat.2020.08.048.
[41] C. Wang, X. Wu, J. Liu, Transmission electron microscopy of martensite/austenite islands in pipeline steel X70, Mater. Sci. Eng. A. 440 (2006) 267–271, https://doi.org/10.1016/j.msea.2006.02.118.